Chapter

Organic/Inorganic Halide Perovskites for Mechanical Energy Harvesting Applications

Venkatraju Jella, Swathi Ippili, Hyun You Kim, Hyun-Suk Kim, Chunjoong Kim, Tae-Youl Yang and Soon-Gil Yoon

Abstract

Organic/inorganic halide perovskites (OIHPs) have recently emerged as promising candidates for the creation of high-efficiency electronic and optoelectronic devices, having superior performance because of their unique features such as excellent optical and electronic properties, cost-effective fabrication, solution-processing, and simple device architecture. The noteworthy dielectric and ferro/piezoelectric properties of OIHPs have enabled the design of mechanical energy harvesters (MEHs). Considerable research has been conducted on using OIHPs in the field of piezoelectric and triboelectric nanogenerators. In this chapter, we describe the potential of OIHP materials, such as organic and inorganic halide perovskites, for harvesting ambient mechanical energy and convert it into electrical energy. Furthermore, the crystal structure of OIHPs along with their dielectric, piezoelectric, and ferroelectric properties are discussed in detail. Recent innovations in OIHP-based MEHs are also summarized. The role of OIHP-polymer composites in enhancing the performance and operational stability of nanogenerators is discussed. Certain issues and challenges facing contemporary OIHP-based MEHs are stated, and finally, some directions for future developments are suggested.

Keywords: OIHP, piezoelectricity, triboelectricity, mechanical energy, nanogenerator

1. Introduction

The rapid progress in artificial intelligence and internet-of-things technologies has increased the demand for portable and sustainable energy sources that can enable perpetual operation [1, 2]. Mechanical energy harvesters (MEHs) that convert abundant mechanical energy from the environment (wind, raindrops, water flow, and vibrations) as well as from human motions (walking, jogging, and running) into electricity, is considered a promising solution to alleviate the energy crisis for supplying power to low-power consumed portable electronics [3]. In particular, piezoelectric nanogenerators (PENGs) and triboelectric nanogenerators (TENGs)

have received immense attention as they efficiently convert mechanical energy into electricity for powering portable and wearable electronics [4]. Furthermore, their simple structure, easy fabrication process, high energy-conversion efficiencies, flexibility, and mechanical robustness makes them well-suited for energy generation [4, 5]. PENGs transform mechanical energy into electricity by generating electric dipoles through the deformation of piezoelectric materials, while TENGs convert mechanical energy into electricity effectively through a coupling of contact electrification and electrostatic induction. In the past decade, several flexible MEHs have been demonstrated using diverse piezoelectric nanostructured materials including ceramics (e.g., $PbZr_xTi_{1-x}O_3$ (PZT) and $BaTiO_3$), semiconductors (e.g., ZnO and CdS), and polymers (PVDF and its derivatives) [6–9]. Among these materials, perovskite-structured ceramics (i.e., ferroelectric materials) are commonly used materials for constructing efficient PENGs and sensors because of their strong dielectric and ferroelectric/piezoelectric properties [10, 11].

In recent years, organic/inorganic halide perovskites (OIHPs) have emerged as promising materials for solar cells with extremely high-power conversion efficiencies over 25% because of their unique optical and electrical properties while having a simple solution process [12]. Besides the discovery of the intriguing ferroelectric and piezo-electric properties of OIHPs have accelerated their recent application in PENGs [13–15]. In 2016, the first thin-based PENG was reported based on the solution-processed ferroelectric $MAPbI_3$ thin films [14]. Subsequently, several flexible PENGs based on OIHP thin films and OIHP–polymer composite films have been developed [13]. OIHPs also exhibit impressive dielectric properties, which is one of the essential features for fabricating efficient TENGs. The first TENG based on $MAPbI_3$ displayed light-dependent triboelectric output characteristics with a moderate performance [15]. Later, a series of commonly used Cs-based perovskites were applied in TENGs owing to their stability compared to organic perovskites [16, 17]. The light-active nature along with the ferro/piezoelectric properties of OIHP harnesses the light-dependent output characters of PENGs as well as TENGs, which allows the nanogenerators to be used as bimodal sensors for sensing pressure and light [18].

In this chapter, we introduce the viability of OIHP materials for mechanical energy harvesting in the form of nanogenerators. The crystal structure and dimensionality of OIHPs along with their dielectric, piezoelectric, and ferroelectric properties are discussed in detail. In addition, the operating mechanisms of OIHP based-MEHs (PENG and TENG) are discussed. Furthermore, the recent progress of various MEHs based on a broad range of OIHP/OIHP–polymer composite materials is summarized. Finally, a brief glimpse into current challenges and future developments for OIHP-based nanogenerators is provided.

2. Structure and dimensionality of OIHPs

The term "perovskite" represents a class of materials originating from the mineral calcium titanate ($CaTiO_3$) and having a crystal structure of ABO_3, which were discovered in 1839 by Gustav Rose [19]. Oxide perovskites are widely used in various dielectric, ferroelectric, piezoelectric, and pyroelectric applications. However, OIHPs differ from inorganic ceramic perovskites by containing halide anions in place of oxide anions. Three-dimensional (3D) OIHPs also have the general crystal structure of ABX_3 (**Figure 1a**) [20], in which A represents an organic or inorganic monovalent cation (e.g., methylammonium ($MA^+ = CH_3NH_3^+$), formamidinium ($FA^+ = CH (NH_2)_2$), or
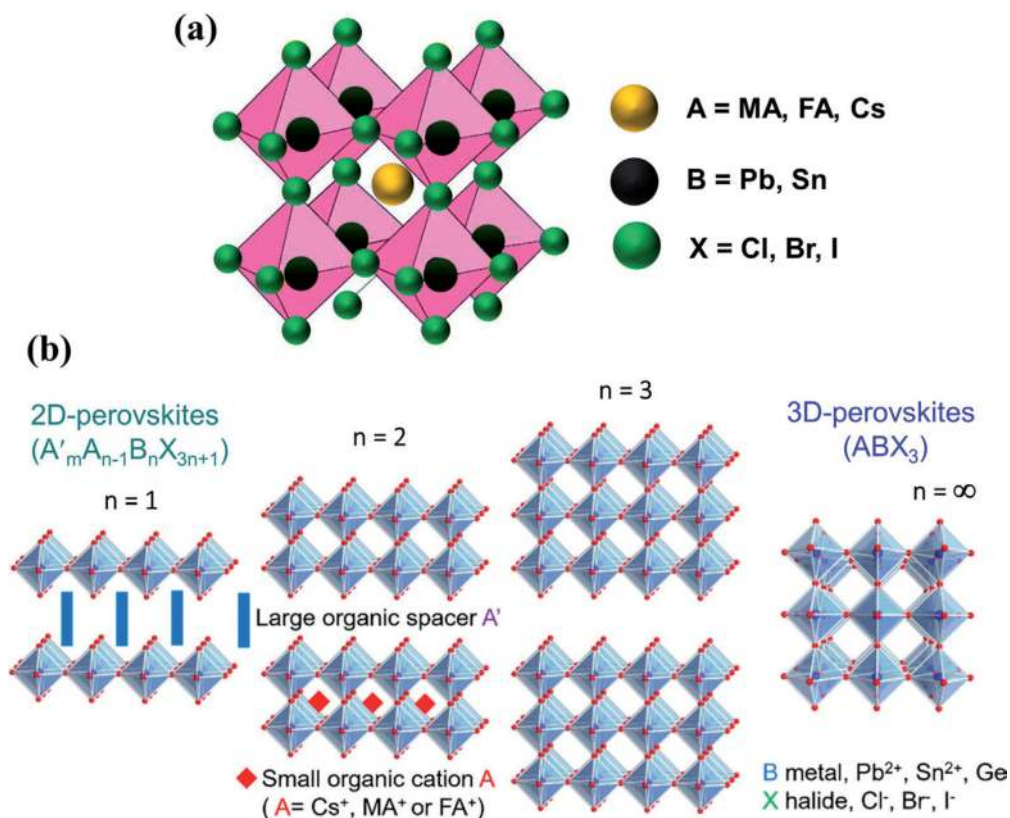
Figure 1.
Schematic representation of a) typical ABX_3 type 3D OIHP structure, b) structures of 2D OIHPs of $A'_mA_{n-1}Bn_X3_{n+1}$ (with the value of n increasing from n = 1 to n = ∞) [24].

cesium (Cs^+)), B denotes a divalent metal cation (e.g., Pb^{2+} or Sn^{2+}), and X indicates a halide anion (Cl, Br, and I). In the crystal structure, A-site cations are connected with 12 neighboring X, while B-site is coordinated by 6 X anions to form cuboctahedral and BX_6 octahedral geometries, respectively. The formation of the perovskite structure and its stability can be evaluated by the Goldschmidt tolerance factor (t) and the octahedral factor (μ) [21]. The tolerance factor is given by t = $(r_A + r_X)/\sqrt{2}(r_B + r_X)$, where r_A, r_B, and r_X are the ionic radii of A, B, and X, respectively. The octahedral factor is given by μ = r_B/r_X, which is directly correlated with a BX_6 octahedron. The tolerance factor and octahedral factor values of OIHPs are expected to be in the range of 0.813 < t < 1.107 and 0.44 < μ < 0.90 [13], respectively. OIHPs tend to form ideal cubic, orthorhombic, and hexagonal structures when 0.8 < t < 1.0, t < 0.8, and t > 1, respectively [13, 22]. 2D perovskites or layered perovskites are formed by intro-ducing large organic functional groups into the 3D structure (**Figure 1b**) and have received immense attention because of their excellent ambient stability [23]. These 2D perovskites can be prepared using a mixture of small cations that forms perovskite and a large organic cation that forms the layered metal halide. The general chemical formula for these layered perovskites is $A'_mA_{n-1}B_nX_{3n+1}$, where A′ is a monovalent (m = 2) or divalent (m = 1) long-chain organic cation (e.g., aromatic or aliphatic alkylammonium), which acts as a spacer. A, B, and X are cations and anions similar to the ones in 3D OIHPs, and n specifies the number of perovskite layers. Here, n = ∞ corresponds to a 3D structure, n = 1 represents a 2D structure, and other values of n denote a quasi-2D structure [24].

3. Structure and dimensionality of OIHPs

3.1 Dielectric properties

A dielectric is referred as an insulating material that is polarized under an applied external electric field. The response of a dielectric material to an applied field is expressed in terms of permittivity. The dielectric constant or relative permittivity (ε_r) of a material is usually obtained from the ratio of its permittivity to the permittivity of a vacuum (ε_0). Materials having a large dielectric constant have the ability to develop higher polarization for an applied electric field. In general, inorganic materials are well-known dielectric materials. In recent times, OIHPs are attracting extensive attention to be used as dielectric materials because of their simple low-temperature synthesis process. ABX_3-structured materials exhibit higher dielectric constant values owing to the ease of polarizing the cell structure. Specifically, distortion of the edge-sharing BX_6 octahedra in the ABX_3 structure can produce an electric dipole between the A and B sites. OIHPs demonstrate impressive dielectric properties analogous to ceramic perovskites, but the values are relatively lower owing to the existence of polar organic cations in the center of the perovskite structure, which can introduce orientational disorder and polarization. The dielectric properties of various lead (Pb) and lead-free OHIPs have been previously investigated experimentally [14, 25, 26]. Kim et al. measured the temperature-dependent dielectric properties of $MAPbI_3$ thin films and confirmed their tetragonal-cubic phase transition. $MAPbI_3$ revealed a dielectric constant value of 52 at 100 kHz [14]. Furthermore, structural tuning of $MAPbI_3$ also affects its dielectric properties. For example, with the partial incorporation of Cl into $MAPbI_3$, the dielectric constant of the resultant films increased to 90.9 at 100 kHz (**Figure 2a**), while Br-incorporated $MAPbI_3$ films exhibited a dielectric constant of 71.6 at 100 kHz [25]. In addition, a structural transition was also observed for partially incorporated Fe^{2+} into $MAPbI_3$ from the dielectric study [26]. The partial replacement of Pb^{2+} with Fe^{2+} ions exhibited a tetragonal–cubic phase transition
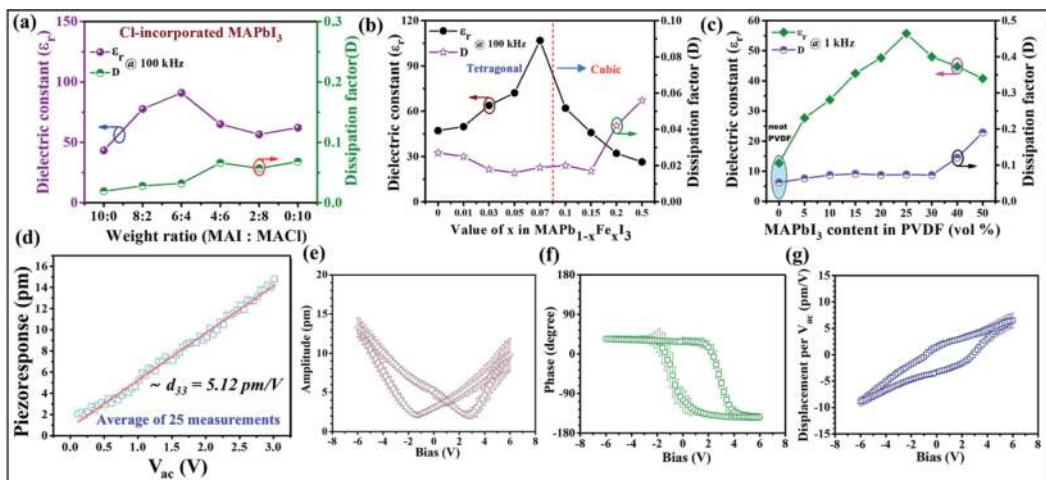

Figure 2.
Dielectric constants and dissipation factors of a) Cl-doped $MAPbI_3$ thin films [25], b) Fe^{2+}-incorporated $MAPbI_3$ thin films, c) $MAPbI_3$-PVDF composite films, e) Piezoelectric response in $MAPbI_3$ thin films, and Piezoelectricity in $MASnBr_3$ thin films; e) Piezo-amplitude, f) Piezo-phase hysteresis loop, and g) Piezo-response [30].

as discovered by the frequency dielectric study of Fe^{2+}-incorporated $MAPbI_3$ thin films (**Figure 2b**). The dielectric constant (ε_r) at 100 kHz of $MAPb_{1-x}Fe_xI_3$ films continuously increased as the Fe^{2+} content increased to x = 0.07, attaining a maximum value of 107. It then decreased for larger Fe^{2+} content, indicating the ferroelectric-to-paraelectric phase transition for x = 0.07. The dielectric properties of OHIP-polymer composites were also investigated by a few researchers. In general, the heterogeneous materials interfaces in polymer composite films can induce an interfacial or a Maxwell–Wagner–Sillars polarization that results in an abrupt change of the total dielectric constant [27, 28]. As the $MAPbI_3$ content in PVDF polymer increased, the dielectric constant of the $MAPbI_3$–PVDF composite rapidly increased because of large dipole–dipole interactions (**Figure 2c**) [29]. In addition, the interaction between the organic action of MA^+ and $-CF_2-$ between the perovskite and PVDF leads to the self-orientation of polymer chains, enabling the nucleation of the electroactive phase that results in the formation of a spontaneous polar β-phase in the composite films. Similarly, the dielectric properties of lead-free $MASnBr_3$–PDMS composite films were also examined for various percentage weights of $MASnBr_3$ (0 to 25 wt.%) [30]. As the $MASnBr_3$ increased from 5 to 15 wt.% content, the dielectric constants of composite films progressively increased and achieved a maximum of 36.23 for 15 wt.% at 1 kHz. By contrast, the dielectric constant values of composite films decreased with a higher loading amount of $MASnBr_3$ owing to increased agglomeration of $MASnBr_3$ particles, which leads to the leaky nature of composite films. The tuning of the dielectric and piezoelectric properties of OIHPs by a simple solution process makes them suitable to be used to construct efficient mechanical energy harvesters.

3.2 Piezoelectric properties

The piezoelectric effect refers to the capability of certain materials to generate electric charges under applied mechanical stress, which is also known as the direct piezoelectric effect. Conversely, an electric field applied to the material induces mechanical strain, which is called the converse piezoelectric effect. This unique property of piezoelectric materials allows their use as sensors and actuators. The structural requirement for a material to exhibit piezoelectricity is non-centrosymmetric. Piezoelectricity was first demonstrated in 1880 by brothers Pierre and Jacques Curie. The direct piezoelectric effect is observed in many natural crystalline materials such as Rochelle salt, quartz, topaz, and human bone. In addition, many engineered materials, in particular, inorganic perovskite materials with a structure of ABO_3 including PZT, $BaTiO_3$ and $(K,Na)NbO_3$, exhibit a noticeable piezoelectric effect, and are widely studied for several applications [6]. The piezoelectric response or piezoelectric energy-harvesting capability of any piezoelectric material can be determined by its piezoelectric coefficient and is proportional to the dielectric constant and polarization (i.e., $d_{33} \propto \varepsilon_r P_r$) [13].

OIHPs also exhibit relatively good piezoelectric properties similar to inorganic ceramic perovskites, but the values are comparatively lower. In recent years, some researchers have investigated the piezoelectric properties of OIHPs in order to determine their potential in various device applications. Kim et al. investigated the piezoelectric coefficient (d_{33}) of solution-processed polycrystalline $MAPbI_3$ films using piezoresponse force microscopy (PFM) and reported a d_{33} of 5.12 pm/V [14] (**Figure 2d**). A single-crystalline device may provide direct evidence regarding the piezoelectric properties of OIHPs, whereas studying the piezoelectric properties of

polycrystalline films using PFM could face challenges owing to inaccurate estimation of tip contact area and other artifacts arising from surface topography and crystal orientation [27]. In this regard, Dong et al. verified the piezoelectric effect in single-crystalline $MAPbI_3$ by depositing two parallel facet gold electrodes [28]. They obtained a d_{33} of 2.7 pm/V along the (001) direction for single-crystal $MAPbI_3$ using the laser interferometry method. Compositional tuning of OIHPs also substantially altered their piezoelectric properties. The partial replacement of Pb with Fe in $MAPbI_3$ improved the d_{33} of 17.0 ± 6.0 pm/V for $MAPb_{1-x}Fe_xI_3$ (x = 0.07) [26]. Similarly, there was a considerable improvement in d_{33} of 20.8 pm/V observed for lead-free $MASnI_3$ by substituting Sn in the Pb-site in $MAPbI_3$ [31]. Likewise, lead-free $MASnBr_3$ perovskite displayed a d_{33} of 2.7 pm/V [30] (**Figure 2e–g**). The slanted butterfly shape in amplitude loop of the $MASnBr_3$ is caused from the electrochemical properties of defects, vacancies, and ions, which indicate that the $MASnBr_3$ possess both electrochemical and piezoelectric properties. According to Ding et al., replacing the A and X site in $MAPbI_3$ with FA and Br, respectively, significantly increased d_{33} (25 pm/V) for $FAPbBr_3$ having a particle size 50–80 nm, which is a five-fold enhancement over $MAPbI_3$ [32]. In addition, inorganic $CsPbBr_3$ films also revealed a higher d_{33} of 40.3 pm/V after poling than organic $MAPbI_3$ films [33]. As a subclass of 3D OIHPs, the piezoelectric properties of 2D perovskites (vacancy-ordered double perovskites) are also recently attracting significant research attention owing to their excellent ambient stability compared to 3D OIHPs. Although 2D OIHPs exhibit superior ambient stability, very few piezoelectric studies have been focused on the recently evolved 2D OIHPs. For instance, solution-processed $(ATHP)_2PbX_4$ displayed ferroelectric behavior with a large d_{33} of 76 pC/N and a giant piezoelectric voltage co-efficient (g_{33}) of 660.3 × 10^{-3} V.m/N [34]. In addition, most 2D OIHPs have ferroelectric natures, thus displaying superior piezoelectric properties as a subclass of piezoelectric materials.

3.3 Ferroelectric properties

Ferroelectric materials are a class of dielectric materials that exhibit ferroelectricity. Ferroelectricity is the ability of materials to possess spontaneous electric polarization and originates from a non-centrosymmetric crystal structure. The direction of spontaneous polarization can be reversed in accordance with an applied external electric field. Ferroelectric materials belonging to the perovskite family (ABX_3 crystal structure) are a subclass of pyroelectric and piezoelectric materials. Ferroelectric materials show ferroelectric behavior only below the Curie temperature (T_C). Above T_C, these materials display the paraelectric state (i.e., they are only polarized under an applied electric field). For example, a well-known inorganic perovskite, $BaTiO_3$, undergoes a structural transition from tetragonal to cubic above 393 K [35]. Recently, OIHPs have been studied specifically with a focus on their ferroelectric properties because of their structural transition and impressive dielectric properties. Although there is a debate on existing ferroelectricity in $MAPbI_3$, several researchers have conducted theoretical and experimental investigations to search for evidence of ferroelectricity in OIHPs. For instance, Kutes et al. provided the first experimental evidence of ferroelectricity in solution-processed $MAPbI_3$ thin films with a grain size of ~100 nm by directly observing the ferroelectric domains through a PFM study, which is a necessary tool to observe the ferroelectric domains at nanometer resolution. The reversible switching of those ferroelectric domains was also realized by electrical poling with a DC bias [36]. Rakita et al. conducted an experimental

investigation for the existence of ferroelectricity in tetragonal MAPbI$_3$. They observed the polarization inversion under an external field, lack of inversion symmetry, and spontaneous polarization based on the measurements of a polarization-electric field (P-E) hysteresis loop, second harmonic generation signals, and pyroelectric response, respectively [37]. Kim et al. confirmed the tetragonal-to-cubic phase transition by measuring temperature-dependent dielectric properties [14]. These studies clearly indicate the experimental evidence for ferroelectricity in MAPbI$_3$ films. In addition, the PFM study upon lead-free MASnI$_3$ demonstrates its ferroelectric property (**Figure 2e–g**) [31]. From the PFM results, a well-defined butterfly-shaped hysteresis loop and the existence of 180° of domain switching validate ferroelectric polarization in MASnI$_3$ films. However, commonly used 3D OIHPs including MAPbI$_3$ and MASnI$_3$ exhibit relatively low T$_C$, limiting their wider applicability at high temperature. Pan et al. reported stable 3D (3-ammoniopyrrolidinium) RbBr$_3$[(AP)RbBr$_3$] perovskites synthesized by evaporation of the precursor's solution, which exhibited a ferroelectric nature at a high Tc = 440 K (**Figure 3**) [38].

Recently, researchers have been keen to study the ferroelectric properties of 2D OIHPs having advantageous characteristics including structural flexibility, diversity, and excellent moisture stability. The large asymmetric A-site cation
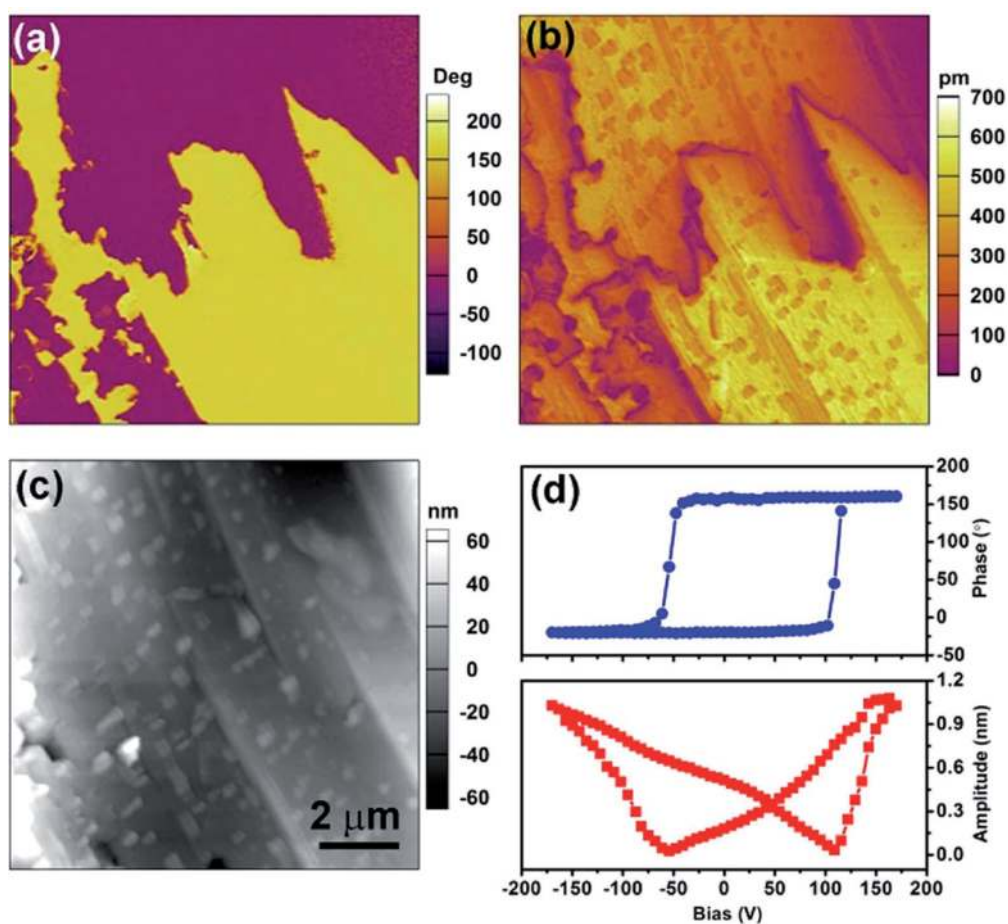

Figure 3.
PFM analysis of 2D layered (ATHP)$_2$PbBr$_4$ films; a) lateral PFM phase, b) amplitude, c) corresponding topography images and d) obtained local piezoelectric response phase hysteresis (top) and amplitude (bottom) loops under applied DC-bias [34].

provides an additional asymmetry to the 2D OIHP crystal. The orientation of such a large cation promotes ferroelectricity. Many excellent 2D OIHPs were designed and their ferroelectric properties investigated. For instance, 2D $(ATHP)_2PbBr_4$ was synthesized using the simple solution method and its ferroelectric property was investigated by measuring the P-E curve and lateral PFM [34]. The 180° contrast of domain orientation in the PFM phase image and separation of the adjacent domains by the domain walls in the PFM amplitude are a direct indictor of ferroelectricity for $(ATHP)_2PbBr_4$ (**Figure 4**). Another 2D OIHP [$(4,4\text{-DFHHA})_2PbI_4$ (4,4-DFHHA=4,4-difluorohexahydroazepine)] displayed ferroelectric properties with a spontaneous polarization of 1.1 μC/cm^2 at room temperature, with a T_C of 454 K [39].

4. MEHs based on OIHPs

A mechanical energy harvester that can produce electricity from mechanical vibrations is a very promising tool to realize sustainable energy generation in remote/indoor environs and even through human body movements. MEHs generally operate based on either the piezoelectric effect, triboelectric effect, or electromagnetic induction effects [13]. Amongst them, PENGs that operate based on piezoelectric effect and TENGs that operate based on triboelectric effect have attracted intense attention because of their direct power conversion ability and relatively easier fabrication processes. Intense research efforts have been conducted with regard to material and structural design, functionality, operation mechanism, and performance optimization of PENGs and TENGs [8, 13, 18]. More recently, the unique properties, low-temperature solution processing, and tunability of properties via compositional-tuning of OIHPs have highlighted their superior potential in the field of mechanical energy harvesters.

4.1 The working mechanism of a PENG

The working mechanism of a general piezoelectric nanogenerator having the metal–insulator–metal structure along with the formation of dipoles under applied force is schematically portrayed in **Figure 4**. In a non-poled piezoelectric material, the dipoles will be randomly orientated, while the orientation of those dipoles will be changed according to the applied electric field direction under poling. Initially, there
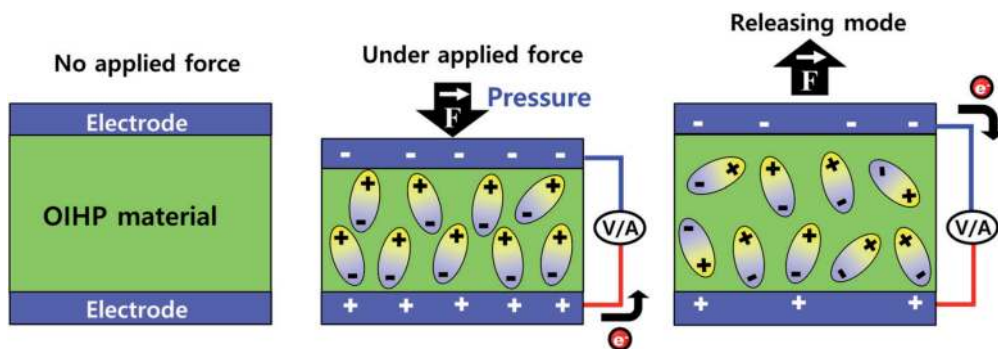

Figure 4.
Schematic illustration of working mechanism of OIHP-based PENG.

will be no generation of output from the PENG without any applied strain owing to the absence of potentials (or in equilibrium state) at the electrodes. However, when mechanical stress is applied normal to the PENG, the piezoelectric material undergoes compressive deformation leading to the generation of dipoles within the active material. The subsequent dipolar polarization results in a piezoelectric potential difference between the two electrodes of the nanogenerator. This, in turn, leads to the flow of charges from one electrode to the other electrode through the external circuit by producing an electrical output signal. When the applied force is withdrawn, the piezoelectric potentials vanish and the electrons flow back to the original position and generate an electrical output signal with the opposite polarity. This output generation is a cyclic process under applied cyclic pressures. In addition, the output of a PENG significantly depends on the material and also some external parameters like applied pressure and frequency.

4.2 The working mechanism of a TENG

A TENG can effectively transform the irregular and randomly distributed mechanical energy into usable electricity via coupling contact electrification with electrostatic induction [18]. In general, when two different materials are in contact with each other, chemical bonds will be formed between the interface of those materials, leading to charge (i.e., electrons, or ions, or molecules) transfer from one material to another because of the difference in their electron affinities [40]. When the two surfaces are separated from each other, the potential drop in the triboelectric charges induces charges into the electrodes via electrostatic induction effect. The potential difference between the electrodes drives electrons to flow between the two electrodes, thus generating triboelectricity form the devices. Based on this principle, four kinds of TENGs with different modes of operations have been developed, as shown in **Figure 5**. In the contact–separation mode, the first invented operation mode of TENG, two dielectric films are placed face to face, and metal electrodes are deposited on the opposite surfaces of the dielectric layers (**Figure 5a**). The TENG operates when the force is applied normal to the device. In the lateral sliding mode, the device structure is similar to that of contact–separation mode (**Figure 5b**), and the TENG operates when the two films keep sliding against one another. This sliding operation offers more efficient charge transfer compared to that offered by the contact–separation mode [41]. By contrast, single-electrode mode is designed to work independently and can be moved freely (**Figure 5c**). This mode is composed of a moving dielectric film and an electrode film connected to the ground. When the top dielectric film approaches towards and/or departs from the bottom electrode, the distribution of the local electrical field may change by generating a potential difference between electrode and ground. This leads to a flow of electrons between the ground and electrode and generates electricity. The freestanding triboelectric-layer mode consists of two symmetrical electrodes underneath a moving dielectric layer that has electrodes of similar sizes (**Figure 5d**). In this mode of operation, no direct physical contact between the two triboelectric layers can be realized, which tends to extend the lifetime of the TENG [42]. Among these modes, the OIHP-based TENGs developed so far were constructed and operated based on vertical contact–separation mode [43, 44]. In the OIHP-based TENGs, the OIHP film fabricated on the electrode-coated substrate is a triboelectric material and is naturally separated from the counter triboelectric material using spacers. Furthermore, when a piezoelectric material like OIHP is used to construct a TENG, the dipoles formed by mechanical deformation of a piezoelectric material under an applied force promote the
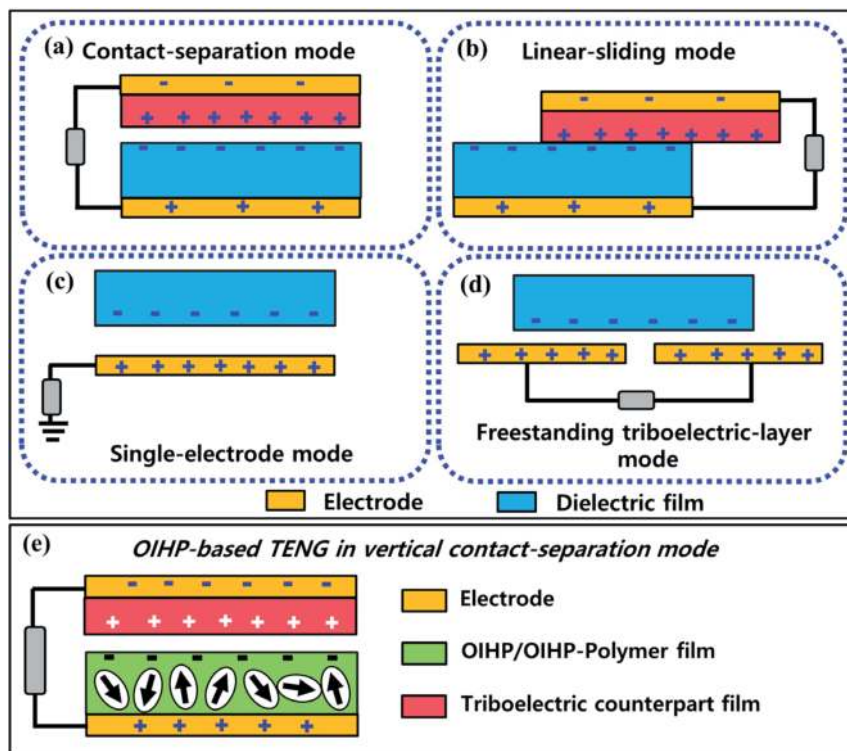
Figure 5.
Schematic depiction of a–d) the four fundamental operating modes of TENG, e) vertical contact–separation mode of OIHP/OIHP-polymer composite based TENG.

generation of more charges onto the surface of the OIHP film during TENG operation, as schematically portrayed in **Figure 5e** [8].

4.3 OIHP-based PENGs

OIHP materials have only been recently applied to PENGs because of their favorable characteristics, which include high piezoelectricity, flexibility, large-area fabrication and low-temperature synthesis along with the biocompatibility of lead-free OIHPs [30, 31]. In addition, various OIHP-polymer composite materials were developed to achieve flexible PENGs with improved mechanical and air stability [29]. Although the output power of OIHP PENGs is very moderate and is lower than OIHP solar cells, with increasing research efforts, the output power has enormously increased with polymer composites. OIHP-based PENGs having the typical metal–insulator–metal structures similar to other piezoelectric materials based devices and were constructed on flexible plastic substrates using simple solution methods [45, 46]. Yoon et al. reported the first OIHP PENG using solution-processed MAPbI$_3$ thin films as shown in **Figure 6a**. The PENG poled at an applied field of 80 kV/cm demonstrated an output voltage and current density of ~2.7 V and ~140 nA/cm^2 under a mechanical pressure of 0.5 MPa (**Figure 6b**) [14]. Later, many researchers focused on improving the output performance of OIHP PENGs [25, 26, 47]. For example, the lateral-structured PENG with inter digitated electrode (IDE) patterns using a MAPbI$_3$ active layer and ZnO & Cu$_2$O-charge transport layers achieved improved output current values [47]. The device was poled under a low (12 kV/cm) electric field for 10 min and was
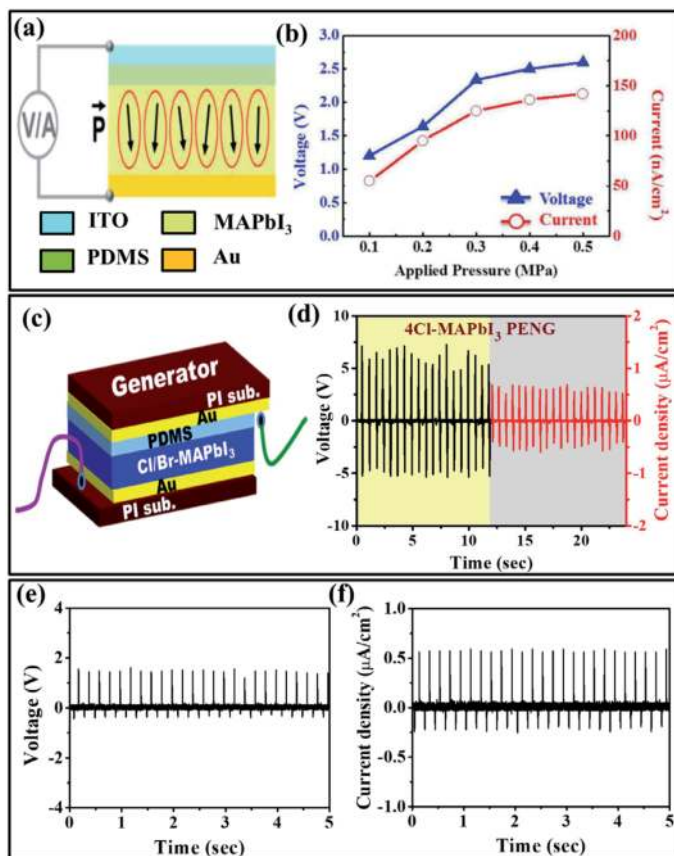
Figure 6.
a) Schematic picture of MAPbI₃-based PENG, and b) corresponding pressure-dependent piezoelectric output performance [14]. c) Schematic depiction of Cl/Br-doped MAPbI₃ PENG, and d) piezoelectric output performance of 4Cl-doped MAPbI₃ PENG [25]. Piezoelectric output performance of MASnBr₃ PENG: e) output voltage and f) current density signals [30].

able to generate a voltage of ~1.47 V and a current of ~0.56 μA under 0.2 MPa pressure. In addition, the output of OIHP PENGs can be further enhanced by controlling the dielectric and piezoelectric properties of perovskite material via the concept of functional-modification of perovskite. A high amount of Cl or Br doping into MAPbI₃ perovskite leads to enhanced dielectric and piezoelectric properties, which results in better piezoelectric output performance from halide doped-MAPbI₃ PENGs compared to the pure MAPbI₃ PENG (**Figure 6c**) [25]. As shown in **Figure 6d**, the poled 4Cl-MAPbI₃ PENG generated a particularly high output voltage and current density of ~5.9 V and ~0.61 μA/cm², respectively, because of the improved dielectric constant (ε_r = 90.9) and remanent polarization (P_r = 0.56 μC/cm²) of perovskite film. Similarly, the partial incorporation of Fe^{2+} into the Pb^{2+} sites of MAPbI₃ perovskite using the simple solution method rapidly enhanced the piezoelectric output performances of PENGs [26]. As discussed earlier, with increasing Fe^{2+} content, the morphological and crystalline properties of the $MAPb_{1-x}Fe_xI_3$ thin films were improved, leading to improvement of dielectric and piezoelectric properties up to a doping amount of 7 at.% (x = 0.07). After 10 at.% (x = 0.10) doping, the $MAPb_{1-x}Fe_xI_3$ samples exhibited a structural transition from tetragonal to cubic; this was a paraelectric material and is unsuitable for PENG applications. However, as the Fe^{2+} concentration increased, the piezoelectric output performance of $MAPb_{1-x}Fe_xI_3$ thin-film PENGs linearly increased

and achieved a maximum of 4.52 V for 7 at.%-doped PENG. In addition, the same 7 at.%-doped PENG demonstrated a much higher piezoelectric output of 7.29 V and 0.88 $\mu A/cm^2$ after poling at an applied electric field of 30 kV/cm.

However, the high toxicity of Pb makes it inappropriate for direct application in the human body or real environs. Researchers have been searching for other lead-free materials in an effort to develop alternatives to lead-based nanogenerators. One of the emerging lead-free OIHP materials is Sn-based perovskite, which is eco-friendly, biocompatible, and has a large piezoelectric coefficient comparable to that of ceramic $PbTiO_3$, which makes it a promising candidate for high-performance nanogenerators in the medical field [31, 48]. The poled lead-free $MASnI_3$ PENG produced an output voltage of 3.8 V and a current density of 0.35 $\mu A/cm^2$ under an applied pressure of 0.5 MPa [31]. Similarly, the lead-free $MASnBr_3$ PENG displayed an output voltage and current density of 1.56 V and 0.58 $\mu A/cm^2$, respectively, under the same applied pressure of 0.5 MPa (**Figure 6e** and **f**) [30]. The generated low output from the $MASnBr_3$ film is because of a lower piezoelectric coefficient of 2.7 pm/V compared to the $MASnI_3$ d_{33} value of 20.8 pm/V [30, 31]. In addition to organic–inorganic halide perovskites (OHPs), some researchers have also explored inorganic halide perovskite (IHP) materials for PENG applications because of their decent environment stability compared to OIHPs. In particular, $CsPbX_3$ has attracted considerable interest in device applications given its higher chemical stability than other perovskites. The $CsPbBr_3$ nanogenerator was developed on a plastic substrate with the structure of PET/ITO/PDMS/$CsPbBr_3$/ITO/PET and poled at an applied electric field of 25 kV/cm [33]. The PENG demonstrated better output performance with an output voltage and current of 16.4 V and 604 nA, respectively, after optimized poling conditions. The same device was further able to sense selective motions, such as eye-blinking, throat movements, and finger motions of a human body, highlighting the potential of $CsPbBr_3$ materials for physiological sensing applications.

Although many studies prove the potential of materials in harvesting mechanical energy for generating the electricity, the practical application of OIHP-based PENGs has not been realized so far because of their lower outputs. Furthermore, they are completely incompatible with irregular mechanical deformations. Hence, a key solution proposed was to create composite OIHP structures with polymer materials for the construction of high-performance and long-term air-stable nanogenerators that can withstand highly harsh environs. The first OIHP–PDMS composite-based PENG (PET/ITO/$FAPbBr_3$-PDMS/Al) was developed by incorporating ferroelectric $FAPbBr_3$ nanoparticles into a PDMS polymer, spin-coating the composite onto an indium tin oxide (ITO)-coated PET substrate, and integrating the film with Al foil acting as a top electrode [32]. This PENG demonstrated a maximum piezoelectric output voltage and current density of 8.5 V and 3.8 $\mu A/cm^2$, respectively, under pushing. Another group developed an eco-friendly PENG using lead-free $MASnBr_3$-PDMS composite material (**Figure 7a**), which displayed a high piezoelectric output voltage of 18.8 V, current density of 13.76 $\mu A/cm^2$, and power density of 74.52 $\mu W/cm^2$ under an applied pressure of 0.5 MPa (**Figure 7b**) [30]. In addition, the PENG exhibited enormous air-stability over 120 days and mechanical durability over more than 10,000 cycles. However, the non-uniform dispersion of perovskite materials in highly viscous polymers like PDMS may result in modest interactions between PDMS and perovskite crystals that could reduce the piezoelectric output performance of nanogenerators [13]. Soon after, researchers have made use of ferroelectric PVDF polymers to realize high-performance nanogenerators because of its ferroelectric nature [29, 49–52].
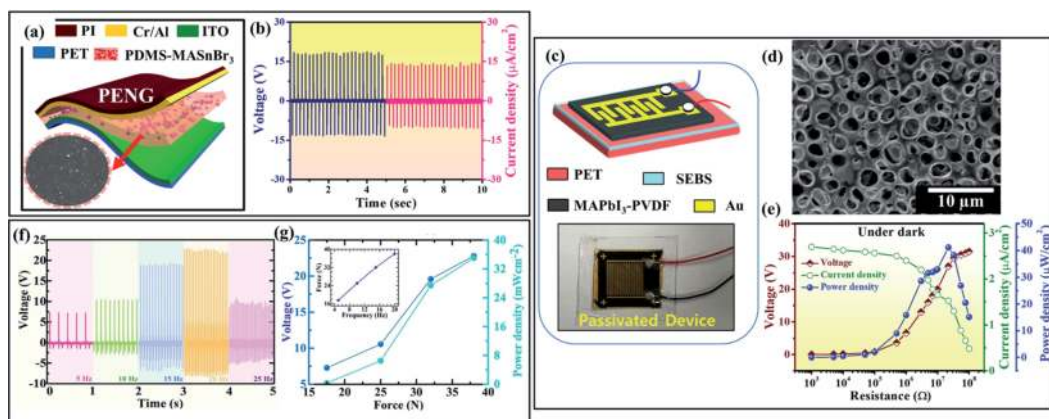
Figure 7.
a) Schematic representation of MASnBr$_3$-PDMS composite based PENG, and b) corresponding piezoelectric output performance [30]. c) Schematic diagram of MAPbI$_3$-PVDF composite based PENG (inset is fabricated device), d) SEM image of 25 vol% MAPbI$_3$-PVDF composite film, and e) corresponding load-resistance dependent piezoelectric output performance [52]. f) Frequency-dependent piezoelectric output voltage signals of FASnI$_3$-PVDF composite PENG and g) Force-dependent piezoelectric output voltage and power densities of FASnI$_3$-PVDF composite PENG and [50].

PVDF, a semi-crystalline ferroelectric polymer, is mainly available in four phases (α, β, γ, and δ). Among these, the β-phase is one of the polar phases and is a highly electroactive phase with superior piezoelectric properties [49]. Hence, the MAPbI$_3$ perovskite solution was mixed with PVDF solution and spin-coated onto the desired plastic substrates to construct PENGs (**Figure 7c**) [52]. The 25 vol% MAPbI$_3$-PVDF composite films showed porous-like morphology with good dispersion of MAPbI$_3$ nanoparticles into the PVDF matrix as shown in SEM image of **Figure 7d** [29, 52]. By increasing the volume fraction of MAPbI$_3$, the dielectric and ferroelectric properties of composite films improved remarkably owing to the enhanced β-phase content of the PVDF matrix caused by the strong polar interactions or hydrogen bonding between MAPbI$_3$ and PVDF. In addition, PVDF encapsulation significantly increased the air-stability of MAPbI$_3$ perovskite over 6 months [29]. The 25 vol% MAPbI$_3$-PVDF PENG, with the IDE-structure given in **Figure 7c**, generated a high piezoelectric output voltage, current density and power density of 33.6 V and 3.54 μA/cm^2, 41.18 μW/cm^2, respectively, at an applied pressure of 300 kPa, while demonstrating long-term operational stability and mechanical stability due to SEBS polymer passivation (**Figure 7e**) [52]. Furthermore, another eco-friendly PENG based on lead-free FASnI$_3$-PVDF nanocomposite materials that has a high piezoelectric coefficient of 73 pm/V demonstrated a piezoelectric output voltage of 23 V [50]. The piezoelectric output of the same PENG is highly influenced by the applied frequency and force as shown in **Figure 7f** and **g**, respectively. Furthermore, the developed lateral-structured PENGs based on highly uniform CsPbBr$_3$-PVDF composite fibers reveal a recordable piezoelectric output performance with an output voltage of 103 V and circuit current of 170 μA/cm^2, which is noticeably higher than many OIHP/OIHP-polymer materials [51]. The same composite PENG exhibits enhanced thermal/water/acid–base stabilities along with exceptional mechanical stability. These results open up a route for more simple and cost-effective production of high-performance PENGs using OIHPs and their polymer composite materials for mechanical energy harvesting and sensor applications.

4.4 OIHP-based TENGs

TENGs have been intensively utilized as flexible power sources and self-powered sensors [8]. Two dissimilar triboelectric nature materials lying at the extreme opposite ends of the triboelectric series are usually employed to fabricate TENGs in order to achieve higher output power. In particular, materials with high dielectric properties are suitable for realizing efficient TENGs, which are designed as part of capacitors [8]. Therefore, OIHPs are recognized as one of the most promising candidates for developing efficient TENGs because of their remarkable dielectric and piezoelectric properties along with low-temperature synthesis [52]. The first OIHP-based TENG developed using $MAPbI_3$ perovskite is operated as a self-powered photodetector based on the combined properties of photoelectric and triboelectric effects [15]. The TENG comprising of two triboelectric parts (Cu/PET as a negative triboelectric material and $MAPbI_3$/TiO_2/FTO as a positive triboelectric material) as illustrated in **Figure 8a** is operated in a fundamental vertical contact–separation mode. This TENG generated a triboelectric peak-to-peak output voltage of 8 V under mechanical pushing in darkness because of triboelectrification. The output is immediately decreased by nearly 37.5% (~5 V) under illumination with a light-intensity of 100 mW/cm^2, giving rise to a high responsivity of 7.5 V/W due to photogenerated charges in the light-active $MAPbI_3$ film (**Figure 8b**). Further, the compositional tuning and electrical poling of perovskite materials can significantly improve the triboelectric performance of TENGs, because compositional modification and ion migration under poling process both tend to alter the conductivity of the OIHP films, which in turn changes the surface potential and electron affinity of those films [43]. Clearly, as shown in **Figure 8c**, the conductivity of the $MAPbI_3$ perovskite film can noticeably change to either p-type (MAI rich) or n-type (PbI_2 rich) by regulating the MAI/PbI_2 ratio during the precursor synthesis [43]. This concept can further extend to TENG applications to realize high-performance TENGs. The composition-tuned $MAPbI_3$ perovskite is paired with PTFE and nylon (PA6) polymer films to develop TENGs (**Figure 8d**). Here, the
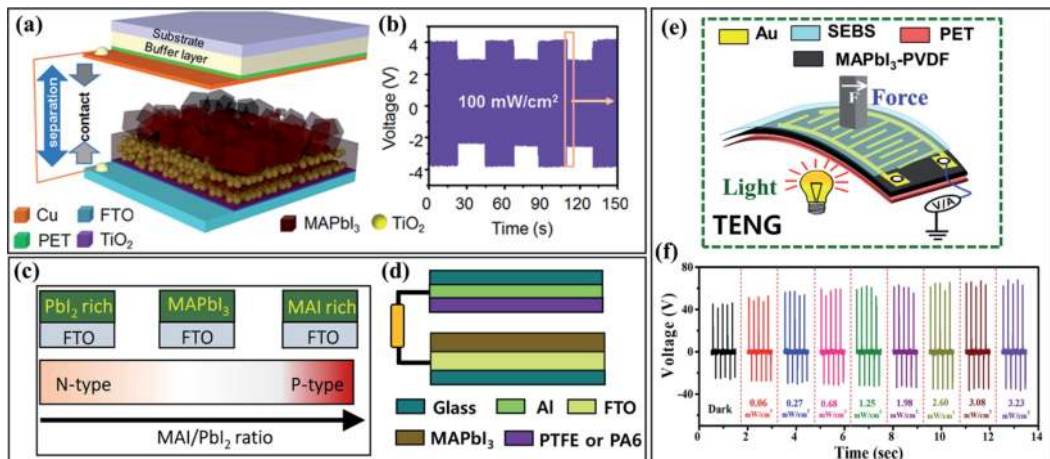

Figure 8.
a) Schematic representation of $MAPbI_3$-based TENG, and b) corresponding light-dependent triboelectric output performance [15]. c) Schematic illustration of n and p type conversion in $MAPbI_3$ films by controlling of MAI/PbI_2 ratio, and d) schematic diagram of $MAPbI_3$-based TENG with the counter triboelectric parts of PTFE/PA6. e) Schematic drawing of $MAPbI_3$-PVDF composite-based TENG in single-electrode mode operation, f) corresponding light-dependent triboelectric output voltage signals under constant pressure of 300 kPa [52].

500-nm-thick $MAPbI_3$ film acts as a triboelectric positive friction layer while pairing with the triboelectric negative PTFE film in PT-PVK TENG and generates a peak output current density of 61.25 mA/m^2. By contrast, the $MAPbI_3$ film acts as a triboelectric negative friction layer while pairing with the triboelectric positive PA6 in PA-PVK TENG and generates a peak output current density of 21.5 mA/m^2 with opposite polarity compared to that of PT-PVK TENG. The poling process further enhances the triboelectric output of PT-PVK TENG. The device generated a maximum output voltage, current density, and peak power density of 979 V, 106 mA/m^2, and 24 W/m^2 after an optimal compositional tuning (MAI/PbI_2 ratio of 2) and poling process (E_P = 4 V/ μm). Similarly, the TENGs fabricated using composition tuned-Cs based perovskites demonstrate notable variations in their triboelectric output depending upon A-site or B-site, or halogen modification [44]. The TENG (glass/FTO/$CsPbBr_{3-y}Cl_y$//PVDF/Ag) demonstrates increasing output performance with increasing Cl content and reaches an output similar to that of only $CsPbCl_3$-based TENG owing to increased electron-donating ability with increasing doping amount. Here, perovskite acts as a triboelectric positive layer, while PVDF films act as a triboelectric negative layer.

As in the case of the OIHP–polymer PENGs, the OIHPs were further composited with polymer materials to improve the long-term operational stability along with air-stability of OIHP–polymer TENGs. To this end, several TENGs with different structures, materials, and modes of operations were developed and their feasibility to harvest the mechanical energy was demonstrated. The flexible single-structure multifunctional device with the structure of $MAPbI_3$-PVDF/Au-IDE/SEBS can harvest mechanical energy and simultaneously sense multiple external stimuli like light and pressure (**Figure 8e**) [52]. The TENG in a single-electrode mode generates an output voltage of ~44.7 V, a current density of ~4.34 $μA/cm^2$, and a power density of ~59.52 $μW/cm^2$ under cyclic contact–separations in darkness. Furthermore, the triboelectric output gradually increases with increasing light-intensity and reaches a maximum voltage of 67.9 V (**Figure 8f**), current density of 7.44 $μA/cm^2$, and power density of 158.34 $μW/cm^2$ at a high light intensity of 3.23 mW/cm^2. This significant enhancement in triboelectric output is because of the combined photoelectric and triboelectric properties of the $MAPbI_3$–PVDF active layer. Under mechanical pushing, when the pushing stack (Al_2O_3/Al-stack) touches the surface of the SEBS polymer, contact electrification results in the generation of charges with opposite polarities on the surfaces of the pushing stack as well as SEBS polymers. Concurrently, the active piezoelectric $MAPbI_3$–PVDF layer undergoes deformation, thus generating dipoles. Owing to the combined triboelectric and piezoelectric effects, the charges will be induced on the Au electrode, leading to a higher potential difference between the electrode and the ground. The resultant potential difference allows the flow of electrons through the external circuit to the ground, thus generating improved outputs. However, when the TENG is illuminated under the applied pressure, the induced triboelectric charge allows the rapid injection of photogenerated charge carriers from $MAPbI_3$ into the Au electrode. This results in a significantly higher triboelectric output under illumination compared to dark-state. Similarly, the fabricated $MAPbI_3$–PDMS composite e-skin-based TENG is highly capable of harvesting mechanical energy and producing neural-stimulating electrical signals without relying on an external power supply [53]. The triboelectric output performance of e-skin significantly increases as the bending radius increases and shows high output voltage and currents of 0.659 V and 8.94 nA, respectively, for a bending angle of 60°. In addition, the device displays strain-dependent and

light-stimulated voltage variations, which enable the device to operate as a self-powered pressure and physiological sensor application. More recently, a stretchable, breathable, and long-term stable hybrid MEH has been developed based on eco-friendly, 2D layered lead-free $Cs_3Bi_2Br_9$, PVDF-HFP and SEBS composite (LPPS-NFC) nanofibers prepared via an electrospinning process [54]. Here, the strong electron-accepting nature of perovskite materials acts as a nucleating agent and improve the crystallinity and polar β-phase of PVDF polymers. The developed composite nanofibers can efficiently harvest the mechanical energy in piezoelectric as well as triboelectric modes. The LPPS-NFC stretchable device with the structure of Spandex/Ag-SEBS/LPPS-NFC//Al generates much larger peak-to-peak outputs with a voltage of 400 V, current density of 1.63 $μA/cm^2$, and power density of 2.34 W/m^2 in the hybrid mode based on the combined piezoelectric and triboelectric effects of composite film. Furthermore, the LPPS-NFC based MEHs reveal excellent stability and are able to produce stable outputs even under harsh mechanical deformations like washing, folding, and crumpling, indicating the superior potential of these LPPS-NFC-based MEHs for use in smart textile-based wearable devices. All these results demonstrate the high potential of hybrid perovskites as triboelectric materials, given their superior dielectric property and stepping forward for high-performance TENG platforms.

5. Current challenges and future prospects

Plenty of research effort has been expended in the study of OIHP nanogenerators to prove the potential of OIHPs as promising active materials for mechanical energy harvesting. The development of OIHP-based mechanical energy harvesters can substantially advance IoT and AI systems. OIHP nanogenerators can operate as sensors that have a wide range of utility in environment monitoring, health monitoring, motion detection, robotics, e-skin, and human-machine interactions. Furthermore, those nanogenerators can supply power to conventional batteries in small-scale and portable electronic devices. However, the key factors that need to be resolved currently in the field of OIHP-based MEHs are air-stability, encapsulation, toxicity, mechanical sturdiness, and moderate performances. Future developments in this field are likely to be focused on the following aspects. First, the output performance and energy conversion efficiency of OIHP-based MEHs should be improved to meet the requirements of small-scale/portable devices. Second, in order to be implemented in wearable devices, the OIHP nanogenerators should be highly flexible, stretchable, and lightweight, and must be able to withstand harsh environs. Third, the eco-friendly nature and low toxicity of OIHP-based devices is a key characteristic for use in health monitoring/biomedical devices; thus, the need of lead-free OIHPs for MEH applications is necessary. Systematic investigations of OIHPs having various dimensions can introduce a new platform for designing high-performance nanogenerators. Controlling the dielectric and ferro/piezoelectric properties of various OIHPs via compositional and structural engineering can also assist nanogenerators to improve energy conversion efficiencies. Furthermore, it has been recognized that layered 2D OIHPs have better piezo/ferroelectric properties along with decent moisture and air stability compared to the 3D OIHPs owing to the presence of long-chain organic cation molecules. It is expected that flexible and stretchable self-powered systems with dynamic sensing properties are the future direction of wearable electronic devices. Therefore, integrating OIHPs with flexible piezoelectric polymers

will aid in the construction of air-stable, mechanically robust and high-performance nanogenerators.

6. Conclusions

In this chapter, we presented the ability of OIHP materials including organic and inorganic halide perovskite materials to produce electricity by harvesting the ambient abundant mechanical energy. The structural suitability of various OIHPs and OIHP–polymer composites for developing high-performance MEHs is discussed in detail along with their dielectric, piezoelectric, and ferroelectric properties. In addition, some significant works based on OIHP-MEHs in the form of PENGs and TENGs are summarized. Finally, the existing issues and challenges facing current research are stated and some future research directions for pursuing the commercialization of OIHP-based MEHs in wearable, portable electronic devices are suggested.

Acknowledgements

Conflict of interest

The authors declare no conflict of interest.

Author details

Venkatraju Jella*†, Swathi Ippili*†, Hyun You Kim, Hyun-Suk Kim, Chunjoong Kim, Tae-Youl Yang and Soon-Gil Yoon*
Department of Materials Science and Engineering, Chungnam National University, Daejeon, Republic of Korea

*Address all correspondence to: venkatrajujella@gmail.com, iswathirs@gmail.com and sgyoon@cnu.ac.kr

† Both authors contributed equally to this work.

IntechOpen

References

[1] Nižetić S, Šolić P, de Gonzáleze DL, Patrono L. Internet of Things (IoT): opportunities, issues and challenges towards a smart and sustainable future. Journal of Cleaner Production. 2020;**274**:122877. DOI: 10.1016/j. jclepro.2020.122877

[2] Shi Q, Dong B, He T, Sun Z, Zhu J, Zhang Z, et al. Progress in wearable electronics/photonics—moving toward the era of artificial intelligence and internet of things. InfoMat. 2020;**2**:1131-1162. DOI: 0.1002/ inf2.12122

[3] Lee JH, Kim J, Kim TY, Al Hossain MS, Kim SW, Kim JH. All-in-one energy harvesting and storage devices. Journal of Materials Chemistry A. 2016;**4**:7983-7999. DOI: 10.1039/C6TA01229A

[4] Jin DW, Ko YJ, Ahn CW, Hur S, Lee TK, Jeong DG, Lee M, Kang C.-Y, Jung JH: Polarization- and electrode-optimized polyvinylidene fluoride films for harsh environmental piezoelectric nanogenerator applications. Small. 2021;17:2007289. DOI: 10.1002/ smll.202007289

[5] Mao Y, Zhang N, Tang Y, Wang M, Chao M, Liang E. A paper triboelectric nanogenerator for self-powered electronic systems. Nanoscale. 2017;**9**:14499-14505. DOI: 10.1039/ C7NR05222G

[6] Lee H, Kim H, Kim DY, Seo Y. Pure piezoelectricity generation by a flexible nanogenerator based on lead zirconate titanate nanofibers. ACS Omega. 2019;**4**:2610-2617. DOI: 10.1021/ acsomega.8b03325

[7] Le AT, Ahmadipour M, Pung S-Y. A review on ZnO-based piezoelectric nanogenerators: Synthesis, characterization techniques, performance enhancement and applications. Journal of Alloys and Compounds. 2020;**844**:156172. DOI: 10.1016/j.jallcom.2020.156172

[8] Ippili S, Jella V, Thomas AM, Yoon C, Jung J-S, Yoon S-G. ZnAl–LDH-induced electroactive β-phase and controlled dielectrics of PVDF for a high-performance triboelectric nanogenerator for humidity and pressure sensing applications. Journal of Materials Chemistry A. 2021;**9**:15993-16005. DOI: 10.1039/D1TA02966E

[9] Lu L, Ding W, Liu J, Yang B. Flexible PVDF based piezoelectric nanogenerators. Nano Energy. 2020;**78**:105251. DOI: 10.1016/j. nanoen.2020.105251

[10] Luo Y, Szafraniak I, Zakharov ND, Nagarajan V, Steinhart M, Wehrspohn RB, et al. Nanoshell tubes of ferroelectric lead zirconate titanate and barium titanate. Applied Physics Letters. 2003;**83**:440-442. DOI: 10.1063/1.1592013

[11] Jiang W, Zhang R, Jiang B, Cao W. Characterization of piezoelectric materials with large piezoelectric and electromechanical coupling coefficients. Ultrasonics. 2003;**41**:55-63. DOI: 10.1016/ S0041-624X(02)00436-5

[12] Jeong J, Kim M, Seo J, Cao W. Pseudo-halide anion engineering for α-FAPbI3 perovskite solar cells. Nature. 2021;**592**:381-385. DOI: 10.1038/ s41586-021-03406-5

[13] Jella V, Ippili S, Eom J-H, Pammi SVN, Jung J-S, Tran V-D, et al. A comprehensive review of

flexible piezoelectric generators based on organic-inorganic metal halide perovskites. Nano Energy. 2019;**57**:74-93. DOI: 10.1016/j.nanoen.2018.12.038

[14] Kim YJ, Dang TV, Choi HJ, Park BJ, Eom JH, Song HA, et al. Piezoelectric properties of $CH_3NH_3PbI_3$ perovskite thin films and their applications in piezoelectric generators. Journal of Materials Chemistry A. 2016;**4**:756-763. DOI: 10.1039/C5TA09662F

[15] Su ZX, Zhao HY, Li J, Yuan ZL, Wang GZ, Cao G, et al. High-performance organolead halide perovskite-based self-powered triboelectric photodetector. ACS Nano. 2015;**9**:11310-11316. DOI: 10.1021/acsnano.5b04995

[16] Xie GX, Yang XY, Duan JL, Duan YY, Tang QW. Bulk Pt/CsPbBr3 Schottky junctions for charge boosting in robust triboelectric nanogenerators. Journal of Materials Chemistry A. 2020;**8**:11966-11975. DOI: 10.1039/D0TA04463F

[17] Wang YD, Yang XY, Xu WK, Yu XP, Duan JL, Duan YY, et al. Triboelectric behaviors of inorganic $Cs_{1-x}A_xPbBr_3$ halide perovskites toward enriching the triboelectric series. Journal of Materials Chemistry A. 2020;**8**:25696-25705. DOI: 10.1039/D0TA09982A

[18] Ippili S, Jella V, Thomas AM, Yoon S-G. The recent progress on halide perovskite-based self-powered sensors enabled by piezoelectric and triboelectric effects. Nanoenergy Advances. 2021;**1**:3-31. DOI: 10.3390/nanoenergyadv1010002

[19] Goldschmidt V. M Krystallbau und chemische zusammensetzung. zusammenfassender vortrag, gehalten vor der deutschen chemischen gesellschaftam. 1927;**60**:1263

[20] Yi Z, Ladi NH, Shai X, Li H, Shen Y, Wang M-K. Will organic–inorganic hybrid halide lead perovskites be eliminated from optoelectronic applications? Nanoscale Advances. 2019;**1**:1276-1289. DOI: 10.1039/C8NA00416A

[21] Park N-G. Perovskite solar cells: an emerging photovoltaic technology. Materials Today. 2015;**18**:65-72. DOI: 10.1016/j.mattod.2014.07.007

[22] Li Z, Yang M, Park J-S, Wei S-H, Berry J, Zhu K. Stabilizing perovskite structures by tuning tolerance factor: Formation of formamidinium and cesium lead iodide solid-state alloys. Chemistry of Materials. 2016;**28**:284-292. DOI: 10.1021/acs.chemmater.5b04107

[23] Mao L, Ke W, Pedesseau L, Wu Y, Katan C, Even J, et al. Hybrid Dion–Jacobson 2D lead iodide perovskites. Journal of the American Chemical Society. 2018;**140**:3775-3783. DOI: 10.1021/jacs.8b00542

[24] Mao L, Stoumpos CC, Kanatzidis MG. Two-dimensional hybrid halide perovskites: principles and promises. JAM Chemical Society. 2019;**141**:1171-1190. DOI: 0.1021/jacs.8b10851

[25] Jella V, Ippili S, Yoon S-G. Halide (Cl/Br)-incorporated organic–inorganic metal trihalide perovskite films: Study and investigation of dielectric properties and mechanical energy harvesting performance. ACS Applied Electronic Materials. 2020;**2**:2579-2590. DOI: 10.1021/acsaelm.0c00473

[26] Ippili S, Jella V, Kim J, Hong S, Yoon S-G. Enhanced piezoelectric output performance via control of dielectrics in Fe^{2+}-incorporated $MAPbI_3$ perovskite thin films: Flexible piezoelectric generators. Nano Energy.

2018;**49**:247-256. DOI: 10.1016/j.
nanoen.2018.04.031

[27] Labuda A, Proksch R. Quantitative
measurements of electromechanical
response with a combined optical
beam and interferometric atomic force
microscope. Applied Physics Letters.
2015;**106**:253103. DOI: 10.1063/1.4922210

[28] Dong Q, Song J, Fang Y,
Shao Y, Ducharme S, Huan J. Bioinspired
ferroelectric polymer arrays as
photodetectors with signal transmissible
to neuron cells. Advanced Materials.
2018;**28**:2816. DOI: 10.1002/
adma.201603618

[29] Jella V, Ippili S, Eom J-H,
Choi J, Yoon S-G. Enhanced output
performance of a flexible piezoelectric
energy harvester based on stable
$MAPbI_3$-PVDF composite films. Nano
Energy. 2018;**53**:46-56. DOI: 10.1016/j.
nanoen.2018.08.033

[30] Ippili S, Jella V, Kim J, Hong S,
Yoon S-G. Unveiling predominant air-
stable organotin bromide perovskite
toward mechanical energy harvesting.
ACS Applied Materials & Interfaces.
2020;**12**:16469-16480. DOI: 0.1021/
acsami.0c01331

[31] Ippili S, Jella V, Eom J-H, Kim J,
Hong S, Choi J-S, et al. An ecofriendly
flexible piezoelectric energy harvester
that delivers high output performance
is based on lead-free $MASnI_3$ films and
$MASnI_3$- PVDF composite films. Nano
Energy. 2019;**57**:911-923. DOI: 1016/j.
nanoen.2019.01.005

[32] Ding R, Liu H, Zhang X,
Xiao J, Kishor R, Sun H, et al. Flexible
piezoelectric nanocomposite generators
based on formamidinium lead halide
perovskite nanoparticles. Advanced
Functional Materials. 2016;**26**:7708-7716.
DOI: 10.1002/adfm.201602634

[33] Kim DB, Park KH, Cho YS. Origin
of high piezoelectricity of inorganic
halide perovskite thin films and their
electromechanical energy-harvesting
and physiological current-sensing
characteristics. Energy & Environmental
Science. 2020;**13**:2077-2086.
DOI: 10.1039/C9EE03212F

[34] Chen XG, Song XJ, Zhang ZX, Li PF,
Ge JZ, Tang YY, et al. Two-dimensional
layered perovskite ferroelectric
with giant piezoelectric voltage
coefficient. Journal of the American
Chemical Society. 2020;**142**:1077-1082.
DOI: 10.1021/jacs.9b12368

[35] Smith MB, Page K, Siegrist T,
Redmond PL, Walter EC, Seshadri R,
et al. Crystal structure and the
paraelectric-to-ferroelectric phase
transition of nanoscale $BaTiO_3$. Journal
of the American Chemical Society.
2008;**130**:6955-6963. DOI: 10.1021/
ja0758436

[36] Kutes Y, Ye V, Zhou Y, Pang S,
Huey BD, Padture NP. Direct observation
of ferroelectric domains in solution-
processed $CH_3NH_3PbI_3$ perovskite thin
films. The Journal of Physical Chemistry
Letters. 2014;**5**:3335-3339. DOI: 10.1021/
jz501697b

[37] Rakita Y, Bar-Elli O,
Meirzadeh E, Kaslasi H, Peleg Y,
Hodes G, et al. Tetragonal $CH_3NH_3PbI_3$ is
ferroelectric. Proceedings of the National
Academy of Sciences of the United
States of America. 2017;**114**:E5504.
DOI: 10.1073/pnas.1702429114

[38] Pan Q, Liu Z-B, Tang Y-Y, Li
P-F, Ma R-W, Wei R-Y, et al. A three-
dimensional molecular perovskite
ferroelectric: (3-ammoniopyrrolidinium)
$RbBr_3$. Journal of the American
Chemical Society. 2017;**139**:3954-3957.
DOI: 10.1021/jacs.7b00492

[39] Chen X-G, Song X-J, Zhang Z-X, Zhang H-Y, Pan Q, Yao J, et al. Confinement-driven ferroelectricity in a two-dimensional hybrid lead iodide perovskite. Journal of the American Chemical Society. 2020;**142**(22):10212-10218. DOI: 10.1021/jacs.0c03710

[40] Feng H, Zhao C, Tan P, Liu R, Chen X, Li Z. Nanogenerator for biomedical applications. Advanced Healthcare Materials. 2018;**7**:1701298. DOI: 0.1002/adhm.201701298

[41] Lin L, Wang V, Xie Y, Jing Q, Niu S, Hu Y, et al. Sliding-triboelectric nanogenerators based on in-plane charge-separation mechanism. Nano Letters. 2013;**13**:2916-2233. DOI: 10.1021/nl400738p

[42] Wang S, Niu S, Yang J, Lin L, Wang ZL. Quantitative measurements of vibration amplitude using a contact-mode freestanding triboelectric nanogenerator. ACS Nano. 2014;**8**:12004-12013. DOI: 0.1021/nn5054365

[43] Huang S, Shi L, Zou T, Kuang H, Rajagopalan P, Xu H, et al. Controlling performance of organic-inorganic hybrid perovskite triboelectric nanogenerators via chemical composition modulation and electric field-induced ion migration. Advanced Energy Materials. 2020;**10**:2002470. DOI: 10.1002/aenm.202002470

[44] Yu XP, Wang YD, Zhang JH, Duan JL, Yang XY, Liu LM, et al. Halogen regulation of inorganic perovskites toward robust triboelectric nanogenerators and charging polarity series. Journal of Materials Chemistry A. 2020;**8**:14299. DOI: 10.1039/D0TA05531J

[45] Yoon C, Ippili S, Jella V, Thomas AM, Jung J-S, Han Y, et al. Synergistic contribution of flexoelectricity and piezoelectricity towards a stretchable robust nanogenerator for wearable electronics. Nano Energy. 2021;**91**:106691. DOI: 10.1016/j.nanoen.2021.106691

[46] Ding R, Zhang X, Chen G, Wang H, Kishor R, Xiao J, et al. High-performance piezoelectric nanogenerators composed of formamidinium lead halide perovskite nanoparticles and poly(vinylidene fluoride). Nano Energy. 2017;**37**:126-135. DOI: 10.1016/j.nanoen.2017.05.010

[47] Jella V, Ippili S, Eom, J.H, Kim YJ, Kim HJ, Yoo S-G: A novel approach to ambient energy (thermoelectric, piezoelectric and solar-TPS) harvesting: Realization of a single structured TPS-fusion energy device using $MAPbI_3$. Nano Energy. 2018;52:11-21. DOI: 10.1016/j.nanoen.2018.07.024

[48] Liu S, Zheng F, Grinberg I, Rappe AM. Photoferroelectric and photopiezoelectric properties of organometal halide perovskites. The Journal of Physical Chemistry Letters. 2016;**7**:1460-1465. DOI: 10.1021/acs.jpclett.6b00527

[49] Ueberschlag P. PVDF piezoelectric polymer. Sensor Review. 2001;**21**:118-126. DOI: 10.1108/02602280110388315

[50] Pandey R, Sb G, Grover S, Singh SK, Kadam A, Ogale S, et al. Microscopic origin of piezoelectricity in lead-free halide perovskite: Application in nanogenerator design. ACS Energy Letters. 2019;**4**:1004-1011. DOI: 10.1021/acsenergylett.9b00323

[51] Chen H, Zhou L, Fang Z, Wang S, Yang T, Zhu L, et al. Piezoelectric nanogenerator based on in situ growth all-inorganic $CsPbBr_3$ perovskite nanocrystals in PVDF fibers with long-term stability. Advanced Functional Materials. 2021;**31**:2011073. DOI: 10.1002/adfm.202011073

[52] Ippili S, Jella V, Eom S, Hong S, Yoon S-G. Light-driven piezo- and triboelectricity in organic−inorganic metal trihalide perovskite toward mechanical energy harvesting and self-powered sensor application. ACS Applied Materials & Interfaces. 2020;**12**:50472-50483. DOI: 10.1021/acsami.0c15009

[53] Guan H, Lv D, Zhong T, Dai Y, Xing L, Xue X, et al. Self-powered, wireless-control, neural-stimulating electronic skin for in vivo characterization of synaptic plasticity. Nano Energy. 2020;**67**:104182. DOI: 10.1016/j.nanoen.2019.104182

[54] Jiang F, Zhou X, Lv J, Chen J, Chen J, Kongcharoen H, et al. Stretchable, breathable, and stable lead-free perovskite/polymer nanofiber composite for hybrid triboelectric and piezoelectric energy harvesting. Advanced Materials. 2022;**2022**:2200042. DOI: 0.1002/adma.202200042